Chromatin accessibility maps of chronic lymphocytic leukemia identify subtype-specific epigenome signatures and associated transcription regulatory networks

André F. Rendeiro[1,*], Christian Schmidl[1,*], Jonathan C. Strefford[2,*], Renata Walewska[3], Zadie Davis[3], Matthias Farlik[1], David Oscier[3], Christoph Bock[1,4,5†]

[1]CeMM Research Center for Molecular Medicine of the Austrian Academy of Sciences, Vienna, Austria

[2]Cancer Sciences, Faculty of Medicine, University of Southampton, Southampton, United Kingdom

[3]Department of Molecular Pathology, Royal Bournemouth Hospital, Bournemouth, United Kingdom

[4]Department of Laboratory Medicine, Medical University of Vienna, Vienna, Austria

[5]Max Planck Institute for Informatics, Saarbrücken, Germany

[*] These authors contributed equally to this work

[†] Correspondence: cbock@cemm.oeaw.ac.at

Keywords: Chronic lymphocytic leukemia, chromatin accessibility, epigenome mapping, cancer heterogeneity, hematopoietic malignancies, transcription regulation, gene regulatory networks, machine learning, bioinformatics

Abstract

Chronic lymphocytic leukemia (CLL) is characterized by substantial clinical heterogeneity, despite relatively few genetic alterations. To provide a basis for studying epigenome deregulation in CLL, we established genome-wide chromatin accessibility maps for 88 CLL samples from 55 patients using the ATAC-seq assay. These data were further complemented by ChIPmentation and RNA-seq profiling in ten samples. Based on this dataset, we devised and applied a bioinformatic method that links chromatin profiles to clinical annotations. Our analysis identified sample-specific variation on top of a shared core of CLL regulatory regions. *IGHV* mutation status – which distinguishes the two major subtypes of CLL – was accurately predicted by the chromatin profiles, and gene regulatory networks inferred for *IGHV*-mutated vs. *IGHV*-unmutated samples identified characteristic regulatory differences between these two disease subtypes. In summary, we found widespread heterogeneity in the CLL chromatin landscape, established a community resource for studying epigenome deregulation in leukemia, and demonstrated the feasibility of chromatin accessibility mapping in cancer cohorts and clinical research.

Introduction

Chronic lymphocytic leukemia (CLL) is the most common type of leukemia in the Western world[1]. It is characterized by remarkable clinical heterogeneity, with some patients pursuing an indolent course while others progress rapidly and require early treatment. The diverse clinical course of CLL patients, particularly those that initially present with low disease burden, fuels interest in prognostic biomarkers and personalized therapies[2]. Current clinical biomarkers for CLL include mutational status of the *IGHV* genes[3, 4], *IGHV* gene family usage[5], stereotyped B cell receptors[6, 7], serum markers[8, 9], chromosomal aberrations[10, 11], and somatic mutations[12, 13, 14]. Most notably, *IGHV* mutation status distinguishes between a less aggressive form of CLL with mutated *IGHV* genes (mCLL) and a more aggressive form with unmutated *IGHV* genes (uCLL). Several surrogate biomarkers of *IGHV* mutation status have been described. For example, high levels of *ZAP70* expression appear to be associated with uCLL[15]. In addition to these focused biomarkers, transcriptome profiling has been used to define broader molecular signatures that may improve disease stratification independent of *IGHV* mutation status[16].

Recent genome and exome sequencing projects have identified additional genes that are recurrently mutated in CLL[17, 18], some of which have prognostic significance. Nevertheless, CLL samples carry relatively few genetic aberrations compared to other adult cancers[19], and some patients develop progressive disease despite being classified as "low risk" based on genetic markers, suggesting that non-genetic factors are relevant for CLL etiology and outcome. Several lines of evidence point to a role of epigenome deregulation in CLL pathogenesis: First, somatic mutations have been observed in non-coding regions of the genome, where they appear to induce deregulation of relevant cancer genes[18]. Second, chromatin remodeling proteins such as *ARID1A* and *CHD2* are recurrently mutated in CLL[17, 18], indicating causal links between chromatin deregulation and CLL. Third, aberrant DNA methylation was observed in all studied CLL patients[20, 21, 22], correlated with *IGHV* mutation status, and identified a new subtype (iCLL) that appears to be an intermediate between mCLL and uCLL[20, 23].

While prior studies of epigenome deregulation in primary cancer samples have focused almost exclusively on DNA methylation[24], recent technological advances now make it possible to map chromatin landscapes in large patient cohorts. Most notably, the assay for transposase-accessible chromatin using sequencing (ATAC-seq) facilitates open chromatin mapping in scarce clinical samples[25], and ChIPmentation provides a streamlined, low-input workflow for genome-wide mapping of histone marks and transcription factors[26]. These two assays use a hyperactive variant of the prokaryotic Tn5 transposase, which integrates sequencing adapters preferentially into the DNA of genomic regions with accessible chromatin structure. ATAC-seq gives rise to globally similar results as DNase-seq, sharing its ability to detect footprints of transcription factor binding in the chromatin accessibility landscape[27]. ChIPmentation closely recapitulates the results obtained by more classical chromatin immunoprecipitation followed by sequencing (ChIP-seq) protocols[26]. Both assays work well on scarce patient samples, and they enable fast sample processing on timescales that would be compatible with routine clinical diagnostics.

To establish the feasibility of large-scale chromatin analysis in primary cancer samples, and to provide a basis for dissecting regulatory heterogeneity in CLL, we performed chromatin accessibility mapping using the ATAC-seq assay on a cohort of 88 primary CLL samples derived from 55 patients. Furthermore, for ten of these samples we established histone profiles using ChIPmentation for three histone marks (H3K4me1, H3K27ac, H3K27me3) and transcriptome profiles using RNA-seq. We also developed a bioinformatic method for linking these chromatin profiles to clinical annotations and molecular diagnostics data, and we performed an initial analysis of gene regulatory networks that underlie the major disease subtypes of CLL. In summary, this study provides a publicly available reference dataset and a rich source of testable hypotheses for dissecting CLL biology and pathogenesis.

Results

Chromatin accessibility maps for 88 CLL samples

To map the chromatin accessibility landscape of CLL (Figure 1a), we performed ATAC-seq on 88 purified lymphocyte samples obtained from the peripheral blood of 55 CLL patients. These patients were managed at a single medical center, and they collectively represent the spectrum of clinical phenotypes that are commonly observed in CLL (Supplementary Table 1). Their average age at sample collection was 73 years, and 8% of patients were under treatment when the samples were collected. The majority of samples (58%) had been classified as *IGHV*-mutated as part of routine clinical diagnostics (Supplementary Figure 1 and Supplementary Table 1).

All samples selected for ATAC-seq library preparation contained at least 80% leukemic cells. The libraries were sequenced with an average of 24.7 million fragments, resulting in a dataset comprising a total of 2.2 billion sequenced fragments (Supplementary Table 2). Data quality was high in all cases, with mitochondrial and duplicate read rates in the expected range (mean: 38.5%; standard deviation: 9.2) and the characteristic patterns of nucleosome phasing derived from paired-end data (Supplementary Figure 2).

The individual samples were sequenced with sufficient depth to obtain the majority of chromatin-accessible regions that are detectable in each sample (Supplementary Figure 3). Moreover, by combining data across all 88 samples we approached cohort-level saturation in terms of unique chromatin-accessible regions (Figure 1b), indicating that our cohort is sufficiently large to identify most regulatory regions that are common in CLL samples.

As illustrated for the *BLK* gene locus (Figure 1c), our ATAC-seq dataset can be aggregated into a comprehensive map of chromatin accessibility in CLL. This map comprises 112,298 candidate regulatory regions, of which 11.6% are constitutively open across essentially all CLL samples, whereas 59.1% are open in a sizable proportion of samples (5% to 95% of samples), and 29.3% are unique to only one or very few samples (Supplementary Figure 4a). All data are available for interactive browsing and download from the supplementary website (http://cll-chromatin.computational-epigenetics.org/).

Chromatin-accessible regions in CLL are widely distributed throughout the genome, with moderate enrichment at genes and promoters (Figure 1d and Supplementary Figure 4b). We also observed an enrichment for transcription start sites and enhancer elements when we compared the CLL-accessible regions to epigenome segmentations for CD19+ B cells (Figure 1e and Supplementary Figure 4c), a related cell type for which comprehensive reference epigenome data are publicly available[28]. Nevertheless, we also detected a sizable number of CLL-accessible regions that fall into areas of quiescent or repressive chromatin in the epigenome segmentation of the B cells, suggesting that many of these regions may constitute CLL-specific regulatory elements.

Heterogeneity in the CLL chromatin accessibility landscape

Although the number of constitutively accessible regions in our cohort was relatively low (11.6%, Supplementary Figure 4a), we still observed high consistency between individual samples, and any two samples in our dataset shared 70% to 98% of their chromatin-accessible regions (Supplementary Figure 5a). Conversely, we also observed consistent differences in the ATAC-seq signal intensity between samples, many of which appear to reflect genuine biological differences. To facilitate the gene-by-gene investigation of this heterogeneity, we established the "chromatin accessibility corridor" as a means of aggregating the cohort-level variation into a single intuitive genome browser track (Figure 2a and Supplementary Website). As illustrated by the *PAX5* and *BCL6* gene loci, even where the locations of chromatin accessible regions are shared across most samples, substantial differences in the ATAC-seq intensity levels were observed (Figure 2a).

For a more systematic investigation of chromatin heterogeneity in CLL, we calculated the cohort-level variance for each of the 112,298 regions in the CLL consensus map and linked these regions to nearby genes that they may regulate (see Methods for details). Promoters of genes with a known role in B cell biology and CLL pathogenesis showed significantly reduced variability ($p < 10^{-5}$, Kolmogorov-Smirnov test), suggesting that consistent levels of chromatin accessibility at many of these gene promoters may be important for CLL cells (Supplementary Figure 5b). The observed differences in accessibility were not due to differential representation of CpG islands among the promoters of the gene sets ($p = 0.49$, Fisher's exact test). Moreover, distal enhancer elements were equally variable for genes with and without a biological link to CLL ($p = 0.08$, Kolmogorov-Smirnov test).

Beyond these global trends, the variance and distribution of chromatin accessibility across samples was highly gene-specific (Figure 2b and Supplementary Figure 5c), as illustrated by CLL-linked genes including B cell surface markers (*CD19*), B cell receptor signaling components (*CD79A/B*, *LYN*, *BTK*), common oncogenes (*MYCN*, *KRAS*, *NRAS*), and genes that are recurrently mutated in CLL (*NOTCH1*, *SF3BP1*, *XPO1*, *CDKN1B*)[17, 18, 29].

Unsupervised principal component analysis clearly identified *IGHV* mutation status as the major source of heterogeneity in chromatin accessibility among CLL samples (Figure 2c, Supplementary Figure 6). However, the first two principal components explained only 6.7% and 5.2% of the total variance in the chromatin accessibility dataset, suggesting that many other factors contribute to the observed differences between samples.

The most direct way by which differences in chromatin accessibility may influence disease courses would be through differential regulation of CLL-relevant genes. Therefore, to systematically assess the link between chromatin accessibility and gene expression in our cohort, we performed RNA-seq on ten of the CLL samples with matched ATAC-seq data. A weak positive correlation was observed between chromatin accessibility and gene expression (Pearson's $r = 0.3$; Supplementary Figure 7a), which was highly dependent on the distance of the chromatin-accessible region to the nearest transcription start site (Supplementary Figure 7b).

For chromatin-accessible regions located in the vicinity of genes that were differentially expressed between *IGHV*-mutated (mCLL) and *IGHV*-unmutated (uCLL) samples according to the RNA-seq data, we observed significant differences in chromatin accessibility between the two disease subtypes, which allowed for partial separation between the two disease subtypes (Supplementary Figure 7c). An even stronger separation was observed when we focused our chromatin accessibility clustering on regions that had been identified as differentially methylated between mCLL and uCLL in a prior study of DNA methylation in CLL[20] (Supplementary Figure 7d).

Finally, we assessed whether patterns of differential variability between mCLL and uCLL (i.e., higher levels of heterogeneity in one or the other subtype) may provide insights into the biology of these two disease subtypes. We identified 389 regions that showed a higher degree of variability among mCLL samples, whereas 581 regions were more variable among uCLL samples (Supplementary Figure 8a) – consistent with prior results showing higher gene expression variability among uCLL samples[30]. These differentially variable regions were distributed across a broad range of ATAC-seq intensity values, and they were not a side effect of differences in average chromatin accessibility (Supplementary Figure 8b). Genomic region enrichment analysis using the LOLA software[31] found mCLL-variable regions enriched for B cell specific transcription factor binding (*ATF2*, *BATF*, *BCL6*, *NFKB*, *RUNX3*) and active histone marks (Supplementary Figure 8c). In contrast, uCLL-variable regions were strongly associated with the cohesin complex, including binding sites for *CTCF*, *RAD21*, and *SMC3*.

Disease subtype-specific patterns of chromatin accessibility

To link the CLL chromatin accessibility landscape to clinical annotations and molecular diagnostics data (most notably to the *IGHV* mutation status), we devised a machine learning based method that derives subtype-specific signatures directly from the data (Figure 3a). Focusing on the distinction between mCLL and uCLL, we trained random forest classifiers to predict whether a particular sample is *IGHV*-mutated or *IGHV*-unmutated, using the chromatin accessibility values for all 112,298 regions in the CLL consensus map as input. The performance of the resulting classifier was evaluated by leave-one-out cross-validation, and we observed excellent prediction accuracy with a ROC area under curve of 0.96 (Figure 3b), corresponding to a sensitivity of 95.6% at a specificity of 88.2%. In contrast, when we repeated the same predictions 1,000 times with randomly shuffled class labels to control for potential biases in the machine learning analysis, we observed a much lower ROC area under curve close to the theoretical expectation of 0.5 (Figure 3b), which rules out inflated performance due to overtraining.

We extracted the most predictive regions from the trained classifiers, giving rise to a data-driven chromatin signature of mCLL vs. uCLL. Hierarchical clustering categorized these regions into 719 with increased chromatin accessibility in *IGHV*-mutated samples ("mCLL regions", cluster 1 in Figure 3c) and 764 regions with increased chromatin accessibility in *IGHV*-unmutated samples ("uCLL regions", cluster 2 in Figure 3c).

To test whether these differences in chromatin accessibility between mCLL and uCLL reflect broader changes in the epigenome landscape, we performed ChIPmentation for three histone marks, which are associated with regions of open chromatin such as promoters and enhancers (H3K4me1, H3K27ac) and with regions of repressed chromatin (H3K27me3). These experiments were done for ten patients and with the same samples that were used for ATAC-seq, thus allowing for a matched comparison. In mCLL samples, we detected higher levels of the active H3K27ac mark compared to repressive H3K27me3 in those regions that were more accessible in mCLL as opposed to uCLL, and vice versa (Figure 3e). This observation is illustrated by the *ZNF667* promoter and an enhancer at the *ZBTB20* locus (Figure 3d), two genes that have been identified as predictors of time to treatment and overall survival in CLL[32, 33]. We also found that the genes in the vicinity of the signature regions were globally more highly expressed in the cell type in which the chromatin accessibility levels were higher (Figure 3f).

We also analyzed the two differential region sets using LOLA[31] (Figure 3g) and observed that the mCLL regions were enriched for active promoter and enhancer regions (marked by H3K4me1 and H3K27ac) in lymphocyte-derived cell lines (SU-DHL-5, JVM-2, GM12878, and KARPAS-422) as well as binding sites of relevant transcription factors (*BATF*, *BCL6*, and *BLC3*). In contrast, the uCLL regions were enriched for H3K4me1-marked promoter/enhancer regions in CD38-negative naïve B cells, reflecting the postulated naïve B cell origin of these CLL cells[34]. The uCLL regions were also enriched for transcribed regions (H3K36me3) in naïve B cells and in B cell-derived cell lines such as the BL-2 cell line, which has not undergone class-switch recombination.

Linking chromatin-accessible regions to genes, we investigated the enrichment of cellular signaling pathways and observed striking differences (Figure 3h). The mCLL regions were associated with pathways having an established role in normal lymphocytes (CTLA4 inhibitory signaling, high-affinity IgE receptor signaling, Fc epsilon signaling, and Fc gamma receptor signaling), while the uCLL regions were associated with cancer-associated pathways such as NOTCH signaling and FGF receptor signaling.

Finally, we investigated whether a third CLL subtype comprising of *IGHV* intermediate samples (iCLL) could be detected in our dataset, as it was recently proposed based on DNA methylation data[20, 23]. Clustering all samples based on the *IGHV* mutation signature regions, we indeed observed two intermediate clusters, the larger one comprising 21 samples from 14 patients (Figure 3h, green) and the smaller one comprising 3 samples from 2 patients (Figure 3i, brown). Most but not all of these iCLL samples were classified as *IGHV*-mutated based on the molecular diagnostics data (Supplementary Figure 9). Principal component analysis provided further evidence that the chromatin accessibility profiles of these intermediate samples indeed fell between the mCLL and uCLL subtypes (Figure 3j). ChIPmentation as well as RNA-seq analysis also supported their intermediate character, as the observed distribution of histone marks and gene expression were consistently ranging between those observed for the mCLL and uCLL groups (Supplementary Figure 10).

Gene regulatory networks underlying the mCLL and uCLL disease subtypes

On top of chromatin accessibility mapping, ATAC-seq can also provide high-resolution information on transcription factor binding based on their DNA binding footprints[25], which allowed us to infer chromatin-based gene regulatory networks for CLL and its two major disease subtypes (Figure 4a). To that end, we pooled the ATAC-seq data across all analyzed samples, identified footprints for 366 transcription factors with high-quality motifs in the JASPAR database[35], and linked these regulatory elements to their putative target genes (see Methods for details). The quality of the observed footprints was comparable to those in publicly available DNase-seq data for CD19+ B cells (Supplementary Figure 11), although there were some deviations between the two assays that are likely due to the different sequence specificity of the Tn5 enzyme as opposed to the DNase I enzyme.

We first inferred a pan-CLL gene regulatory network using ATAC-seq data from all samples (Supplementary Figure 12). The resulting network was dominated by highly connected transcription factors, including broadly activating factors (*SP1/2/3*), the insulator protein *CTCF*, and regulators of biological processes such as cell proliferation (*EGR*), cell cycle (*E2F*), and B cell maturation (*SPI1*, *PAX5*). This pan-CLL network was structurally similar to a network for CD19+ B cells that we inferred from publicly available DNase-seq data using the same bioinformatic method (Supplementary Figure 13), and in the absence of a large chromatin accessibility dataset of B cells from healthy individuals it is not possible to conclusively identify the CLL-specific parts of our network.

Second, in order to investigate the regulatory differences between CLL subtypes, we inferred gene regulatory networks separately for mCLL and uCLL samples (Supplementary Figure 14) and identified the most differentially connected genes between the two (Figure 4b). Genes that were more highly connected in the mCLL network included the transcription factors *ZNF354C* and *ELF5*, the metallopeptidase *ADAM29*, and the membrane protein *CD22*. In contrast, the BMP receptor CRIM1, the transcription factors *MECOM* and *PAX9*, the FGF signaling receptor *FGFR1*, and the membrane protein *CD9* were more highly connected in the uCLL network (Figure 4c). The more highly connected genes in either subtype also showed higher averages of H3K4me1 and H3K27ac in their regulatory elements in samples of the corresponding subtype (Supplementary Figure 15a, 15b).

When we restricted our analysis to genes with a known role in B cell biology and CLL pathogenesis (Figure 4d), we observed a highly specific association of *CD22* (an inhibitory receptor for B cell receptor signaling) with mCLL, whereas the *CD38* and *ZAP70* genes were preferentially associated with uCLL. Focusing on *CD22* and *PAX9* as two interesting genes emerging from this analysis, we contrasted the sub-networks of their direct neighbors in the gene regulatory networks for mCLL and uCLL (Supplementary Figure 15c), illustrating the characteristic regulatory differences between these two disease subtypes. Finally, many of the subtype-specific genes identified by the regulatory network also showed locus-specific differences in their ChIPmentation profiles (Supplementary Figure 15d), thus providing further support that the analysis identifies relevant differences and illustrating how our dataset can be used for deriving testable hypotheses on the regulatory basis of CLL.

Discussion

By performing ATAC-seq on a large set of primary CLL samples, we have established a detailed map of the chromatin accessibility landscape in CLL. The ATAC-seq data were complemented and validated with RNA-seq and ChIPmentation for three histone marks, each performed in ten representative samples covering three disease subtypes (mCLL, uCLL, iCLL). To our knowledge, this dataset is currently the largest catalog of chromatin accessibility maps for any cancer type, demonstrating the feasibility of chromatin profiling in large cohorts of primary cancer samples.

The large number of patient samples allowed us to dissect the role of epigenome variability as a potential contributor to cancer heterogeneity[36]. We found that variability between samples was widespread in our dataset, but significantly reduced at the promoters of genes with a known role in B cell biology and CLL pathogenesis. Overall, our data support the existence of a core regulatory landscape shared by most or all CLL samples, which is complemented by sample-specific subsets of a substantially larger number of CLL-associated regulatory regions.

IGHV mutation status was the single biggest contributor to sample-specific differences in chromatin accessibility, although it explained only 5-10% of the observed variance in our dataset. Based on the chromatin profiles we were able to distinguish with excellent accuracy between *IGHV*-mutated mCLL and *IGHV*-unmutated uCLL. Our analysis also suggested the existence of one (or possibly two) intermediate types (iCLL), consistent with a recent report that used DNA methylation analysis of a large CLL cohort to identify novel CLL subtypes[20]. Chromatin accessibility and DNA methylation both appear to separate better between these disease subtypes than gene expression data, suggesting that the biological differences between the major subtypes of CLL are primarily encoded in the epigenome and possibly reflect patterns retained from the subtype's corresponding cell-of-origin.

Combining data across samples provided sufficient sequencing depth for footprint analysis of transcription factor binding, allowing us to infer gene regulatory networks from the data and to compare them between mCLL and uCLL. Although genomic footprinting has its limitations[37], these network models give rise to predictions that can provide a starting point for further experimental dissection of the transcription regulatory landscape of CLL. For example, mCLL-associated regions were enriched for transcription factors that are active in mature B cells and involved in memory B cell differentiation (*BATF*, *BCL6*), whereas the uCLL group was enriched for regulatory regions that are active in other hematopoietic cell types, indicative of a less differentiated cell state. Moreover, pathways that may boost proliferation, such as NOTCH signaling[38] and interferon signaling[39], were specifically observed in the more aggressive subtype (uCLL), whereas enrichment of inhibitory signaling by *CTLA4* may contribute to the more indolent character of mCLL[40].

From a technological perspective, our study describes broadly applicable methods for dissecting chromatin profiles in large cohorts of primary patient samples. The differential chromatin analysis outlined in Figure 3 starts from clinical and/or diagnostic data and uses supervised learning techniques to identify and cross-validate discriminatory chromatin signatures. We focused specifically on *IGHV* mutation status, but the method can be applied to any type of patient grouping, for example based on disease progression or therapy response. Moreover, the described method for ATAC-seq based inference of gene regulatory networks (Figure 4) establishes a data-driven approach for dissecting regulatory cell states – including their differences between disease subtypes – that is highly complementary to previous work aimed at inferring regulatory networks from transcriptome data[41 , 42, 43]. Finally, the "chromatin accessibility corridor" provides an adaptation of a related concept[44] and intuitive browser-based visualization for chromatin data across large sample cohorts with significant regulatory heterogeneity.

Relevant limitations of our study include: (i) Lack of a clearly defined and experimentally accessible cell-of-origin for uCLL and mCLL, making it difficult to distinguish with certainty between chromatin patterns that are CLL-specific and those that are derived from the cell-of-origin; (ii) clonal heterogeneity of CLL within patients, which would be experimentally addressable only with single-cell sequencing technologies[45, 46] that are currently limited in their genome-wide coverage; (iii) lack of scalable methods for distinguishing between regulatory and spurious transcription factor binding; and (iv) ambiguities in the assignment of transcription factor binding sites to the genes that they regulate. In the light of these limitations, the inferred gene regulatory networks constitute an initial model that will require future refinement as additional data and validations become available.

In summary, our study establishes a chromatin accessibility landscape of CLL and it identifies widespread regulatory heterogeneity. It also provides a resource that can act as a starting point for deeper dissection of chromatin regulation in CLL, identification of therapeutically relevant mechanisms, and eventual translation of relevant discoveries into clinical practice. Given that the chromatin profiling assays used here (ATAC-seq and ChIPmentation) are sufficiently fast and straightforward for use in a clinical sequencing laboratory, chromatin deregulation is becoming increasingly tractable as a promising source of biomarkers for stratified cancer therapy.

Methods

Sample acquisition and clinical data

All patients were diagnosed and treated at the Royal Bournemouth Hospital (UK) according to the revised guidelines of the International Workshop Chronic Lymphocytic Leukemia/National Cancer Institute (IWCLL/NCI). Patients were selected to reflect the clinical and biological heterogeneity of the disease. Sequential samples were included for a total of 24 patients. All samples contained more than 80% leukemic cells. Established chromosomal rearrangements were diagnosed by fluorescence in situ hybridization (Abbott Diagnostics; DakoCytomation) or multiple ligation dependent probe amplification using the MLPA P037 CLL-1 probemix (MRC Holland SALSA) according to the manufacturers' instructions. Chromosome analysis was performed and reported according to the International System for Human Cytogenetic Nomenclature. *IGHV* was sequenced as previously described[4], and a threshold of >98% germline homology was taken to define the unmutated subset[4]. The study was approved and overseen by the local ethics committee of the contributing institutions.

ATAC-seq

Accessible chromatin mapping was performed using the ATAC-seq method as previously described[25], with minor adaptations. In each experiment, 10^5 cells were washed once in 50 µl PBS, resuspended in 50 µl ATAC-seq lysis buffer (10 mM Tris-HCl, pH 7.4, 10 mM NaCl, 3 mM $MgCl_2$, and 0.1% IGEPAL CA-630) and centrifuged for 10 min at 4°C. Upon centrifugation, the pellet was washed briefly in 50 µl $MgCl_2$ buffer (10 mM Tris, pH 8.0, and 5 mM $MgCl_2$) before incubating in the transposase reaction mix (12.5 µl 2x TD buffer, 2 µl transposase (Illumina) and 10.5 µl nuclease-free water) for 30 min at 37°C. After DNA purification with the MinElute kit, 1 µl of the eluted DNA was used in a qPCR reaction to estimate the optimum number of amplification cycles. Library amplification was followed by SPRI size selection to exclude fragments larger than 1,200 basepairs. DNA concentration was measured with a Qubit fluorometer (Life Technologies). Library amplification was performed using custom Nextera primers[25]. The libraries were sequenced by the Biomedical Sequencing Facility at CeMM using the Illumina HiSeq3000/4000 platform and the 25 basepair paired-end configuration.

RNA-seq

Total RNA was isolated using the AllPrep DNA/RNA Mini Kit (Qiagen). RNA amount was measured using Qubit 2.0 Fluorometric Quantitation (Life Technologies), and the RNA integrity number (RIN) was determined using Experion Automated Electrophoresis System (Bio-Rad). RNA-seq libraries were prepared using a Sciclone NGS Workstation (PerkinElmer) and a Zepyhr NGS Workstation (PerkinElmer) with the TruSeq Stranded mRNA LT sample preparation kit (Illumina). Library amount and quality were determined using Qubit 2.0 Fluorometric Quantitation (Life Technologies) and Experion Automated Electrophoresis System (Bio-Rad). The libraries were sequenced by the Biomedical Sequencing Facility at CeMM using the Illumina HiSeq 3000/4000 platform and the 50 basepair single-read configuration.

ChIPmentation

ChIPmentation was carried out as previously described[26], with minor adaptions. Briefly, cells were washed once with PBS and fixed with 1% paraformaldehyde in up to 1 ml PBS for 10 minutes at room temperature. Glycine was added to stop the reaction. Cells were collected at 500 x g for 10 minutes at 4°C (subsequent work was performed on ice and used cool buffers and solutions unless otherwise specified) and washed twice with up to 0.5 ml ice-cold PBS supplemented with 1 µM PMSF. The pellet was lysed in sonication buffer (10 mM Tris-HCl, pH 8.0, 1 mM EDTA, pH 8.0, 0.25% SDS, 1x protease inhibitors (Sigma), 1 µM PMSF) and sonicated with a Covaris S220 sonicator for 20-30 minutes in a milliTUBE or microTUBE until the size of most fragments was in the range of 200-700 basepairs. Lysates were centrifuged at full speed for 5 minutes at 4°C, and the supernatant containing the sonicated chromatin was transferred to a new tube. The lysate was then brought to RIPA buffer conditions (final concentration: 10 mM Tris-HCl, pH 8.0, 1 mM EDTA, pH 8.0, 140 mM NaCl, 1% Triton x-100, 0.1% SDS, 0.1% DOC, 1x protease inhibitors (Sigma), 1 µM PMSF) in a volume of 200 µl/immunoprecipitation For each immunoprecipitation, 10 µl magnetic Protein A (Life Technologies) were washed twice and resuspended in PBS supplemented with 0.1% BSA. The antibody was added and bound to the beads by rotating 2 hours at 4°C. Used antibodies were H3K4me1 (0.5 µg/immunoprecipitation, Diagenode pAb-194-050), H3K27ac (1 µg/immunoprecipitation, Diagenode pAB-196-050), H3K27me3 (1 µg/immunoprecipitation, Millipore 07-499). For control libraries an IP with 2.5 µg of a nonspecific IgG rabbit antibody was used. Blocked antibody-conjugated beads were then placed on a magnet, supernatant was removed, and the sonicated lysate was added to the beads followed by incubation for 3-4 hours at 4°C on a rotator. Beads were washed subsequently with RIPA (twice), RIPA-500 (10 mM Tris-HCl, pH 8.0, 1 mM EDTA, pH 8.0, 500 mM NaCl, 1% Triton x-100, 0.1% SDS, 0.1% DOC,) (twice), and RIPA-LiCl (10 mM Tris- HCl, pH 8.0, 1 mM EDTA, pH 8.0, 250 mM LiCl, 1% Triton X-100, 0.5% DOC, 0.5% NP40) (twice).

Beads were washed once with cold Tris-Cl pH 8.0 to remove detergent, salts, and EDTA. Beads were washed once more with cold Tris-Cl pH 8.0 but the reaction was not placed on a magnet to discard supernatant immediately. Instead, the whole reaction including beads was transferred to a new tube, and then placed on a magnet to remove supernatant to decrease tagmentation of unspecific chromatin fragments sticking to the tube wall. Beads were then carefully resuspended in 25 µl of the tagmentation reaction mix (10 mM Tris pH 8.0, 5 mM MgCl2, 10% v/v dimethylformamide) containing 1 µl Tagment DNA Enzyme from the Nextera DNA Sample Prep Kit (Illumina) and incubated at 37°C for 1-3 minutes in a thermocycler. The beads were washed with RIPA (twice) and once with cold Tris-Cl pH 8. Beads were washed once more with cold Tris-Cl pH 8.0 but the reaction was not placed on a magnet to discard supernatant immediately. Instead, the whole reaction including beads was again transferred to a new tube, and then placed on a magnet to remove supernatant to remove unspecific tagmented chromatin fragments. Beads were then incubated with 70 µl elution buffer (0.5% SDS, 300 mM NaCl, 5 mM EDTA, 10 mM Tris-HCl pH 8.0) containing 2 µl of Proteinase K (NEB) for 1 hour at 55°C and 8 hours at 65°C to revert formaldehyde crosslinking, and supernatant was transferred to a new tube. Finally, DNA was purified with SPRI AMPure XP beads (sample-to-beads ratio 1:2) or Qiagen MinElute columns.

1 µl of each library was amplified in a 10-µl qPCR reaction containing 0.15 µM primers, 1× SYBR Green and 5 µl Kapa HiFi HotStart ReadyMix (Kapa Biosystems) to estimate the optimum number of enrichment cycles with the following program: 72°C for 5 min; 98°C for 30 s; 24 cycles of 98°C for 10 s, 63°C for 30 s; and 72°C for 30 s; and a final elongation at 72°C for 1 min. Kapa HiFi HotStart ReadyMix was incubated at 98°C for 45 s before preparation of all PCR reactions (qPCR and final enrichment PCR) to activate the hot-start enzyme for successful nick translation in the first PCR step. Final enrichment of the libraries was performed in a 50 µl reaction using 0.75 µM primers and 25 µl Kapa HiFi HotStart ReadyMix. Libraries were amplified for N+1 cycles, where N is equal to the rounded-up Cq value determined in the qPCR reaction. Enriched libraries were purified with size selection using SPRI AMPure XP beads at a beads-to-sample ratio of 1:1, followed by a size selection using AMPure XP beads to recover libraries with a fragment length of 200-400 basepairs. Library preparation was performed using custom Nextera primers as previously described for ATAC-seq[25]. The libraries were sequenced by the Biomedical Sequencing Facility at CeMM using the Illumina HiSeq3000/4000 platform and the 50 basepair single-read configuration.

Preprocessing of the ATAC-seq data

Reads were trimmed using Skewer[47]. Trimmed reads were aligned to the GRCh37/hg19 assembly of the human genome using Bowtie2[48] with the "–very-sensitive" parameter. Duplicate reads were removed using sambamba *markdup*[49], and only properly paired reads with mapping quality >30 and alignment to the nuclear genome were kept. All downstream analyses were performed on the filtered reads. Genome browser tracks were created with the *genomeCoverageBed* command in BEDTools[50] and normalized such that each value represents the read count per basepair per thousand filtered reads. Finally, the UCSC Genome Browser's *bedGraphToBigWig* tool was used to produce a bigWig file. Combined tracks with percentile signal across the cohort were created by quantifying ATAC-seq read coverage at every reference genome position using BEDTools *coverage* and normalizing it between samples. Normalization was done by dividing each value by the total number of filtered reads and multiplying it with 10 million, in order to obtain numbers that are comparable and easy to visualize. Next, the mean as well as the 5th, 25th, 75th and 95th percentiles of signal across the whole cohort were calculated with Numpy, converted into bedgraph files, and subsequently to bigwig format using *bedGraphToBigWig*. Peak calling was performed with MACS2[51] using the "–nomodel" and "–extsize 147" parameters, and peaks overlapping blacklisted features as defined by the ENCODE project[52] were discarded.

Preprocessing of the RNA-seq data

Reads were trimmed with Trimmomatic[53] and aligned to the GRCh37/hg19 assembly of the human genome using Bowtie1[54] with the following parameters: -q -p 6 -a -m 100 --minins 0 --maxins 5000 --fr --sam --chunkmbs 200. Duplicate reads were removed with Picard's *MarkDuplicates* utility with standard parameters prior to transcript quantification with BitSeq[55] using the Markov chain Monte Carlo method and standard parameters. To obtain gene-level quantifications, we assigned the expression values of its highest expressed transcript to each gene. Differential gene-level expression between the three *IGHV* mutation status groups was performed using DESeq2[56] from the raw count data with a significance threshold of 0.05.

Preprocessing of the ChIPmentation data

Reads were trimmed using Skewer[47]. Trimmed reads were aligned to the GRCh37/hg19 assembly of the human genome using Bowtie2[48] with the "–very-sensitive" parameter. Duplicate reads were removed using sambamba *markdup*[49], and only properly paired reads with mapping quality >30 and alignment to the nuclear genome were kept. All downstream analyses were performed on the filtered reads. Genome browser tracks were created with the *genomeCoverageBed* command in BEDTools[50] and normalized such that each value represents the read count per basepair per thousand filtered reads. Finally, the UCSC Genome Browser's *bedGraphToBigWig* tool was used to produce a bigWig file.

Bioinformatic analysis of chromatin accessibility

The CLL consensus map was created by merging the ATAC-seq peaks from all samples using the BEDTools[50] *merge* command. To produce Figure 1b, we counted the number of unique chromatin-accessible regions after merging peaks for each sample in an iterative fashion, randomizing the sample order 1,000 times and computing 95% confidence intervals across all iterations. The chromatin accessibility of each region in each sample was quantified using Pysam, counting the number of reads from the filtered BAM file that overlapped each region. To normalize read counts across samples, we performed quantile normalization using the *normalize.quantiles* function from the preprocessCore package in R. For each genomic region we calculated the support as the percentage of samples with a called peak in the region, and we calculated four measures of ATAC-seq signal variation across the cohort: mean signal, standard deviation, variance-to-mean ratio, and the squared coefficient of variation (the square of the standard deviation over the mean). Additionally, we used BEDTools *intersect* to annotate each region with the identity of and distance to the nearest transcription start site and the overlap with Ensembl gene annotations (promoters were defined as the 2,500 basepair region upstream of the transcription start site). Annotation with chromatin states was based on the 15-state genome segmentation for CD19+ B cells from the Roadmap Epigenomics Project[57] (identifier: E032). To summarize the chromatin accessibility signals into one value per gene (Figure 2b and Supplementary Figure 5b, 5c) we used the accessibility values of the closest region (but no further than 1,000 basepairs from the transcription start site) to represent the promoter, and the mean values of all distal regions (located more than 2,500 basepairs from the transcription start site) of each gene to represent distal regulatory elements. To test for overrepresentation of CpG islands in the promoters of genes with a known role in B cell biology and/or CLL pathogenesis, we downloaded the position of CpG islands in the

GRCh37/hg19 assembly from the UCSC Genome Browser[58], counted the number of promoters (as defined above) that overlapped by at least one basepair with CpG islands in the gene set of interest and in all other genes with accessible elements in CLL, and used Fisher's exact test to assess the significance of the association. Unsupervised principal component analysis was performed with the scikit-learn[59] library (*sklearn.decomposition.PCA)* applied to the chromatin accessibility values of all chromatin-accessible regions across the CLL cohort. To investigate variability within the mCLL and uCLL sample groups, we divided the samples in two groups based on their *IGHV* mutation status (samples below a 98% homology threshold were considered mutated and samples with missing values for the *IGHV* mutation status were excluded from the analysis), and we used the F test from the *var.test* function in R on the chromatin accessibility values of all CLL cohort regions. Significantly variable regions were defined as having a Bonferroni-corrected p-value below 0.05 and mean accessibility above 1. Region set enrichment analysis was performed on the significantly variable regions of each group using LOLA[31] with its core databases: transcription factor binding sites from ENCODE[52], tissue clustered DNase hypersensitive sites[60], the CODEX database[61], UCSC Genome Browser annotation tracks[58], the Cistrome database[62], and data from the BLUEPRINT project[63].

Machine learning analysis of disease subtypes

Random forest classifiers from the scikit-learn[59] Python library (*sklearn.ensemble.RandomForestClassifier*) were trained with the samples' *IGHV* mutation status as class label and the chromatin accessibility values for each sample at each of the 112,298 consensus regions as input features (prediction attributes). All samples with known *IGHV* mutation status were used for class prediction, the performance was evaluated by leave-one-out cross-validation, and the results were plotted as ROC curves using scikit-learn. Given that several patients contributed more than one sample to the cohort, in each iteration of the cross-validation we removed any samples from the training set that belonged to the same patient as the sample in the test set, in order to eliminate a potential risk of overtraining. Furthermore, we repeated the cross-validation 1,000 times based on randomly shuffled class labels to reconfirm that no overtraining occurred in our analysis. The most predictive regions for *IGHV* mutation status were selected by averaging the feature importance of the random forest classifiers over all iterations of the cross-validation and selecting those features with Gini importance higher than 10^{-4}. Region set enrichment was performed using LOLA[31] as described above. Pathway enrichment analysis was performed using seq2pathway[64]. The sample clustering in Figure 3i was based on the pairwise correlation of ATAC-seq signal in the predictive regions between samples, and the dendrogram was plotted using Scipy's hierarchical clustering function. With the same values of chromatin accessibility from above, we performed principal component analysis on the CLL samples using R's implementation in the *prcomp* function.

Gene regulatory network inference

Transcription factor binding maps as the basis for inferring gene regulatory networks were derived by footprinting analysis using the PIQ software[65] and a set of 366 human transcription factor motifs from the JASPAR database[35]. As previously described[66], we retained only those transcription factors with at least 500 high-purity (>0.7) binding sites overlapping with an ATAC-seq peak. Our scheme for assigning transcription factor binding sites to genes was as follows: Binding sites located in the gene body or in the 2,500 basepair region upstream of its transcription start site were assigned to the overlapping gene(s). Intergenic binding sites were assigned to the gene whose transcription start site was closest to the peak. For this association, we used the Ensembl gene annotation version 75, and we treated non-protein-coding genes in the same way as protein-coding genes. To infer gene regulatory networks, an interaction score was calculated in a similar way as previously described[66]: The interaction score between a transcription factor t and a gene g ($S_{t,g}$) was defined as the sum over all n transcription factor binding sites of t that can be assigned to g:

$$S_{t,g} = \sum_{i=1}^{n} 2 * (P_i - 0.5) * 10^{-\left(\frac{d_{i,g}}{100000}\right)}$$

In this formula P_i is the PIQ purity score and $d_{i,g}$ is the distance of a particular transcription factor binding site i to gene g. This score establishes a unidirectional (transcription factors to genes) and weighted (based on the interaction score) relationship, which provide the edges of the gene regulatory network. We inferred gene regulatory networks for all samples combined and also separately for the two disease subtypes (mCLL and uCLL) based on *IGHV* mutation status. We considered only transcription-factor-to-gene interactions with scores above 1, and in Figure 4b as well as Supplementary Figures 12 and 14 we plotted only nodes with more than 200 connections. For the CD19+ B cell gene regulatory network we used DNase-seq data from the Roadmap Epigenomics Project[57] (identifier: E032). Both the processing of the raw data and the network inference were performed in the same manner as ATAC-seq. The comparison of composition and structural characteristics of the gene regulatory networks inferred from ATAC-seq data for the CLL cohort and from DNase-seq data for CD19+ B cells was performed using functions from the *networkx*[67] library in Python. The inferred networks were visualized using the Gephi software, applying the Force Atlas 2 graph layout with LinLog and hub dissuasion. In order to compare the inferred mCLL and uCLL networks, we divided the degree of each node by the total number of edges in each network to compensate for differences in the absolute number of detected interactions, and we quantified differences by subtracting and log2-transforming this value between networks for each node.

Data availability

The ATAC-seq intensity data are available for interactive browsing and download from the supplementary website (http://cll-chromatin.computational-epigenetics.org/). They are also being submitted to NCBI GEO (accession number pending). The raw sequencing data are being submitted to the EBI EGA for controlled access, in order to protect the privacy of the patients who have donated the samples.

Acknowledgements

We would like to thank all patients who have donated their samples for this study. We also thank Amelie Kuchler and Thomas Penz for expert technical assistance, Johanna Klughammer and Nathan Sheffield for their contributions to the data analysis pipeline, the Biomedical Sequencing Facility at CeMM for assistance with next-generation sequencing, and all members of the Bock lab for their help and advice. Moreover, we would like to thank Ulrich Jäger, Medhat Shehata, Philipp Staber, and Jörg Menche for their comments and for critically reading the manuscript. This work was performed in the context of the BLUEPRINT project (European Union's Seventh Framework Programme grant agreement no. 282510) and the ERA-NET projects EpiMark (FWF grant agreement no. I 1575-B19) and CINOCA (FWF grant agreement no. I 1626-B22). C.S. was supported by a Feodor Lynen Fellowship of the Alexander von Humboldt Foundation. J.C.S. was supported by Bloodwise (11052, 12036), the Kay Kendall Leukaemia Fund (873), Cancer Research UK (C34999/A18087, ECMC C24563/A15581), Wessex Medical Research, and the Bournemouth Leukaemia Fund. C.B. was supported by a New Frontiers Group award of the Austrian Academy of Sciences.

Author contributions

A.F.R., C.S., J.C.S., D.O., and C.B. planned the study; J.C.S., R.W., Z.D., and D.O. provided samples and clinical data; C.S. and M.F. performed the experiments; A.F.R. analyzed the data with contributions from C.S., J.C.S., D.O., and C.B.; C.B. supervised the research; all authors contributed to the writing of the manuscript.

Competing financial interests

The authors declare no competing financial interests.

Figure legends

Figure 1: The chromatin accessibility landscape of chronic lymphocytic leukemia (CLL).

a) ATAC-seq profiling and analysis workflow for establishing patient-specific and cohort-level maps of chromatin accessibility in CLL. **b)** Saturation analysis showing the number of unique chromatin-accessible regions detected across 88 samples and with a total sequencing depth of 2.2 billion ATAC-seq fragments. The narrow blue and green corridors indicate 95% confidence intervals for samples added in random order (1,000 iterations). **c)** Genome browser plot showing ATAC-seq signal intensity for 88 individual CLL samples (top), average signal intensity across the cohort and cohort-level peak calls (center), and reference data from the ENCODE project (bottom). Browsable tracks are available from the supplementary website: http://cll-chromatin.computational-epigenetics.org/. **d)** Absolute (frequency) and relative (fold-change) co-localization of unique chromatin-accessible regions in CLL with gene annotations (left) and chromatin state segmentations for CD19+ B cells from the Roadmap Epigenomics project (right).

Figure 2: Heterogeneity in the chromatin accessibility landscape of CLL.

a) Genome browser plot showing ATAC-seq signal intensity across the CLL cohort in the vicinity of two genes with a known role in B cell biology (*PAX5* and *BCL6*). This cohort-level track uses color-coded percentiles to visualize the observed heterogeneity between samples. The bottom row zooms in on the chromatin accessibility landscape at three specific regulatory regions. **b)** Violin plots showing the cohort-wide distribution of chromatin accessibility at promoters (chromatin-accessible regions located with 2,500 basepairs from the transcription start site) and putative enhancers of genes with a known role in B cell biology and/or CLL pathogenesis. **c)** Unsupervised principal component analysis based on the chromatin accessibility for all 88 samples at each of the 112,298 chromatin-accessible regions in the CLL cohort. Samples are color-coded according to their *IGHV* mutation status, using <98% germline homology as threshold for classifying samples as mutated.

Figure 3: Disease subtype-specific patterns of chromatin accessibility.

a) Methodology for deriving disease subtype-specific patterns of chromatin accessibility: A machine learning algorithm is trained to distinguish between different sample groups (here: *IGHV*-mutated vs. *IGHV*-unmutated), the prediction performance is evaluated by cross-validation, and the most predictive features are obtained by feature extraction from the cross-validated models. **b)** ROC curve summarizing the test set prediction performance (estimated by leave-one-out cross-validation) of a random forest classifier that uses the ATAC-seq dataset to distinguish between *IGHV*-mutated and *IGHV*-unmutated samples. “AUC” refers to the ROC area under curve as a measure of prediction performance, and sensitivity/specificity values are shown for the point on the ROC curve that is closest to the top left corner. The grey lines indicate the performance of 1,000 classifiers trained and evaluated in the same way but with randomly shuffled class labels. **c)** Clustered heatmap based on the most predictive regions extracted from the cross-validated classifiers. **d)** Genome browser plots showing ATAC-seq and ChIPmentation profiles for gene loci with a known role in CLL (*ZNF667* and *ZBTB20*). **e**) Ratio between ChIPmentation signal for active chromatin (H3K27ac) and repressive chromatin (H3K27me3) at mCLL-linked and uCLL-linked regions. **f**) Ratio of gene expression levels between genes linked to mCLL-accessible regions and genes linked to uCLL-accessible regions. **g)** Most highly enriched region sets for mCLL (blue) and uCLL (green) associated regions. **h)** Most highly enriched pathways among genes linked to mCLL (blue) and uCLL (green) regions. **i)** Hierarchical clustering of all CLL samples based the classifiers' most predictive regions. Clusters 1 corresponds to mCLL, cluster 4 to uCLL, and clusters 2 and 3 to iCLL. Samples are colored by *IGHV* mutation status (top) and cluster assignment (bottom). **j)** Principal component analysis for the same data as in panel i.

Figure 4: Gene regulatory networks underlying the mCLL and uCLL disease subtypes.

a) Methodology for deriving gene regulatory networks from ATAC-seq data using transcription factor (TF) footprinting, mapping of transcription factor to genes, and regulatory network inference. **b)** CLL gene regulatory network derived from the data of all 88 samples, showing the most differentially connected genes between uCLL and mCLL (the full network is shown in Supplementary Figure 12). Node size reflects the nodes' total number of connections, and colors indicate the network in which the nodes are more highly connected (mCLL: blue; uCLL: orange). **c)** Relative change in the number of connections between the mCLL and uCLL networks, showing all genes. **d)** Same as panel c, but focusing on 81 genes with a known role in B cell biology and/or CLL pathogenesis.

Supplementary Information

Supplementary Table 1: Clinical annotations of the CLL patient cohort.

Clinical annotations for the patient samples that were analyzed in this study. All patients were diagnosed and treated at the Royal Bournemouth Hospital (UK).

Supplementary Table 2: Summary statistics of the sequencing experiments.

Sequencing statistics for 88 samples with ATAC-seq, 10 samples with ChIPmentation for three histone marks (H3K4me1, H3K27ac, H3K27me3) and one control (IgG), and 10 samples with RNA-seq.

Supplementary Figure 1: The cohort reflects a range of CLL phenotypes encountered in clinical care.

Visualization of clinical annotations for the patient samples that were analyzed in this study.

Supplementary Figure 2: Observed ATAC-seq fragment length distributions indicate high data quality.

Distribution of ATAC-seq fragment lengths for published GM12878 data[12] and for four randomly selected CLL samples from this study. Fragment lengths were inferred based on paired-end sequencing data. The characteristic patterns of nucleosome-associated fragment length are observed in all samples.

Supplementary Figure 3: Sequencing depth yields the majority of ATAC peaks detectable in each sample.

Relationship of the number of sequenced reads (x-axis) and the number of detected chromatin-accessible regions (y-axis), showing the average pattern across all 88 samples (blue line). The corridor indicated in green corresponds to a 95% confidence interval for random subsampling across samples.

Supplementary Figure 4: Chromatin-accessible regions in CLL are enriched for promoters and enhancers.

a) Histogram showing the number of samples in which a given chromatin-accessible region from the CLL consensus map was detected as a significant ATAC-seq peak. **b**) Frequency and enrichment of overlap with Ensembl gene annotation for regions in the CLL consensus map, compared to region sets of identical size and lengths that were randomized 1,000 times across the genome. **c**) Frequency and enrichment of overlap with chromatin state segmentations for CD19+ B cells (data from the Roadmap Epigenomics project), compared to region sets of identical size and lengths that were randomized 1,000 times across the genome.

Supplementary Figure 5: Heterogeneity in chromatin accessibility affects genes related to B cells and CLL.

a) Histogram showing the percentage of chromatin-accessible regions that are shared between any two CLL samples. **b**) Distribution of variance in chromatin accessibility for promoter regions and putative distal regulatory regions across all genes (grey) and for a set of 81 genes with a known role in B cell biology and/or CLL pathogenesis (blue/green). Chromatin accessibility scores were averaged across all regulatory regions assigned to a given gene. **c**) Violin plots of normalized chromatin accessibility values for gene promoters (regions located within 2,500 basepairs of the transcription start site) and distal regulatory elements (regions located at least 2,500 basepairs away from the nearest transcription start site) for the same 81 genes as in panel b).

Supplementary Figure 6: Unsupervised analysis identifies *IGHV* mutation status as a key source of variation.

Principal component analysis based on the chromatin accessibility for all 88 samples at each of the 112,298 chromatin-accessible regions in the CLL cohort. The first five principal components are plotted, and samples are colored according to clinical annotations and molecular diagnostics data (top four rows) as well as the sample processing batch for the ATAC-seq experiments (bottom row).

Supplementary Figure 7: Chromatin accessibility is linked to gene expression and differential methylation.

a) Hexbin scatterplot showing a weak correlation (Pearson's r = 0.33) between gene expression levels and chromatin accessibility values at associated regulatory regions, averaging across ten samples with matched ATAC-seq and RNA-seq data. The color gradient is on a logarithmic scale. **b**) Pearson correlation (top) and significance of the association (bottom) between gene expression levels and chromatin accessibility values at associated regulatory regions, plotted over the distance of the accessible region to the gene's transcription start site. **c**) Mean chromatin accessibility across regulatory regions associated with genes that were upregulated in *IGHV*-mutated or in *IGHV*-unmutated CLL. **d**) Mean chromatin accessibility across regulatory regions overlapping with regions that were hypermethylated in *IGHV*-mutated or in *IGHV*-unmutated CLL[20].

Supplementary Figure 8: Subtype-specific variable regions show characteristic enrichment patterns.

a) Scatterplot of the change in variance-to-mean ratio in chromatin-accessible regions between the mCLL and uCLL sample groups (x-axis) and the significance of variability of each region within each group (y-axis). Blue and orange dots indicate significantly variable regions each of the two sample group. **b)** Scatterplots of mean accessibility (left) and variance-to-mean ratio within each sample group (right). The plot on the left illustrates how significantly variable regions are dispersed across the accessibility range and are thus not strongly coupled with differences in mean accessibility between the groups. The color coding is the same as in panel a). **c)** Most highly enriched region sets that significantly overlap with the differentially variable regions for mCLL (blue) and for uCLL (orange), based on LOLA analysis.

Supplementary Figure 9: Clustering on mCLL/uCLL signature regions reflects *IGHV* mutation status.

Hierarchical clustering of all CLL samples based on sample-wise correlation of chromatin accessibility for the most discriminatory regions identified between the *IGHV*-mutated and the *IGHV*-unmutated disease subtype, complemented by clinical annotations and linking samples from the same patient (curved black lines).

Supplementary Figure 10: mCLL/uCLL signature regions show characteristic histone/expression patterns.

a) Hierarchical clustering and heatmap visualizing the ChIPmentation signal for three histone marks (H3K4me1, H3K27ac, H3K27me3) in ten CLL samples comprising three disease subtypes (mCLL, iCLL, uCLL). Regulatory regions were selected and sorted in the same way as in Figure 3c. **b**) Violin plots showing the distribution of

ChIPmentation levels for each histone mark in the same regulatory regions as in panel a, grouped by disease subtype. **c**) Violin plots showing the ratio between the ChIPmentation signal for histone marks associated with active (H3K4me1, H3K27ac) over repressed (H3K27me3) chromatin. **d**) Mean gene expression values for genes associated with the regulatory regions from panel a, grouped by disease subtype. **e**) Boxplot showing the fold change of genes associated with regulatory elements in cluster 1 (mCLL regions) over genes associated with cluster 2 (uCLL regions), again grouped by disease subtypes. In all panels, significance was assessed using the Mann-Whitney *U* test, and comparisons with *p*-values above 0.05 were labeled as not significant (n.s.).

Supplementary Figure 11: Transcription factor footprints for ATAC-seq and DNase-seq are similar.

Footprinting diagrams showing the frequency of Tn5 transposase insertion events (for ATAC-seq) and DNase I cutting sites (for DNase-seq, based on data for CD19+ B cells from the Roadmap Epigenomics project) across a 500 basepair window around motifs of transcription factors involved in B cell development.

Supplementary Figure 12: Cohort-level gene regulatory network identifies regulator proteins in CLL.

Gene regulatory network of CLL inferred from footprint predictions of transcription factor binding, based on the ATAC-seq data of all CLL samples. Only nodes with more than 200 connections are displayed.

Supplementary Figure 13: B cell (DNase-seq) and CLL (ATAC-seq) networks share similar properties.

a) Structural characteristics of transcription factor nodes in gene regulatory networks inferred from ATAC-seq data for the CLL cohort and from DNase-seq data for CD19+ B cells. **b**) Number of connections for all genes in the two gene regulatory networks (transcription factors are shown in red).

Supplementary Figure 14: Gene regulatory networks for mCLL and uCLL samples are globally similar.

Gene regulatory networks inferred based on the *IGHV*-unmutated samples (uCLL, left) and based on the *IGHV*-mutated samples (mCLL, right). Only nodes with more than 200 are displayed.

Supplementary Figure 15: Disease subtype-specific networks detect differentially regulated genes/regions.

a) Violin plots showing the distribution of ChIPmentation levels for each histone mark in regulatory regions associated with genes that are differentially connected between the subtype-specific networks. **b**) Violin plots showing the ratio between the ChIPmentation signal for histone marks associated with active (H3K4me1, H3K27ac) over repressed (H3K27me3) chromatin. **c**) Subnetworks with the neighbors of PAX9 and CD22, shown separately for the mCLL and uCLL networks. Edge widths indicate the strength of the connection as measured by the interaction score. **d**) ATAC-seq and ChIPmentation signal for three histone marks at representative differentially connected genes between the mCLL and uCLL networks. In panel a and b, significance was assessed using the Mann-Whitney *U* test, and comparisons with *p*-values above 0.05 were labeled as not significant (n.s.).

References

1. Byrd JC, Stilgenbauer S, Flinn IW. Chronic lymphocytic leukemia. *Hematology Am Soc Hematol Educ Program*, 163-183 (2004).

2. Zenz T, Mertens D, Kuppers R, Dohner H, Stilgenbauer S. From pathogenesis to treatment of chronic lymphocytic leukaemia. *Nat Rev Cancer* **10**, 37-50 (2010).

3. Damle RN*, et al.* Ig V gene mutation status and CD38 expression as novel prognostic indicators in chronic lymphocytic leukemia. *Blood* **94**, 1840-1847 (1999).

4. Hamblin TJ, Davis Z, Gardiner A, Oscier DG, Stevenson FK. Unmutated Ig V(H) genes are associated with a more aggressive form of chronic lymphocytic leukemia. *Blood* **94**, 1848-1854 (1999).

5. Tobin G*, et al.* Somatically mutated Ig V(H)3-21 genes characterize a new subset of chronic lymphocytic leukemia. *Blood* **99**, 2262-2264 (2002).

6. Agathangelidis A*, et al.* Stereotyped B-cell receptors in one-third of chronic lymphocytic leukemia: a molecular classification with implications for targeted therapies. *Blood* **119**, 4467-4475 (2012).

7. Rossi D*, et al.* Stereotyped B-cell receptor is an independent risk factor of chronic lymphocytic leukemia transformation to Richter syndrome. *Clin Cancer Res* **15**, 4415-4422 (2009).

8. Di Giovanni S, Valentini G, Carducci P, Giallonardo P. Beta-2-microglobulin is a reliable tumor marker in chronic lymphocytic leukemia. *Acta Haematol* **81**, 181-185 (1989).

9. Hallek M*, et al.* Elevated serum thymidine kinase levels identify a subgroup at high risk of disease progression in early, nonsmoldering chronic lymphocytic leukemia. *Blood* **93**, 1732-1737 (1999).

10. Dohner H*, et al.* Genomic aberrations and survival in chronic lymphocytic leukemia. *N Engl J Med* **343**, 1910-1916 (2000).

11. Rossi D*, et al.* Integrated mutational and cytogenetic analysis identifies new prognostic subgroups in chronic lymphocytic leukemia. *Blood* **121**, 1403-1412 (2013).

12. Baliakas P*, et al.* Recurrent mutations refine prognosis in chronic lymphocytic leukemia. *Leukemia* **29**, 329-336 (2015).

13. Oscier DG*, et al.* The clinical significance of NOTCH1 and SF3B1 mutations in the UK LRF CLL4 trial. *Blood* **121**, 468-475 (2013).

14. Stilgenbauer S*, et al.* Gene mutations and treatment outcome in chronic lymphocytic leukemia: results from the CLL8 trial. *Blood* **123**, 3247-3254 (2014).

15. Crespo M*, et al.* ZAP-70 expression as a surrogate for immunoglobulin-variable-region mutations in chronic lymphocytic leukemia. *N Engl J Med* **348**, 1764-1775 (2003).

16. Ferreira PG*, et al.* Transcriptome characterization by RNA sequencing identifies a major molecular and clinical subdivision in chronic lymphocytic leukemia. *Genome Res* **24**, 212-226 (2014).

17. Landau DA*, et al.* Mutations driving CLL and their evolution in progression and relapse. *Nature* **526**, 525-530 (2015).

18. Puente XS*, et al.* Non-coding recurrent mutations in chronic lymphocytic leukaemia. *Nature* **526**, 519-524 (2015).

19. Lawrence MS*, et al.* Mutational heterogeneity in cancer and the search for new cancer-associated genes. *Nature* **499**, 214-218 (2013).

20. Kulis M*, et al.* Epigenomic analysis detects widespread gene-body DNA hypomethylation in chronic lymphocytic leukemia. *Nat Genet* **44**, 1236-1242 (2012).

21. Landau DA*, et al.* Locally disordered methylation forms the basis of intratumor methylome variation in chronic lymphocytic leukemia. *Cancer Cell* **26**, 813-825 (2014).

22. Oakes CC*, et al.* Evolution of DNA methylation is linked to genetic aberrations in chronic lymphocytic leukemia. *Cancer Discov* **4**, 348-361 (2014).

23. Queiros AC*, et al.* A B-cell epigenetic signature defines three biologic subgroups of chronic lymphocytic leukemia with clinical impact. *Leukemia* **29**, 598-605 (2015).

24. Baylin SB, Jones PA. A decade of exploring the cancer epigenome - biological and translational implications. *Nat Rev Cancer* **11**, 726-734 (2011).

25. Buenrostro JD, Giresi PG, Zaba LC, Chang HY, Greenleaf WJ. Transposition of native chromatin for fast and sensitive epigenomic profiling of open chromatin, DNA-binding proteins and nucleosome position. *Nat Methods* **10**, 1213-1218 (2013).

26. Schmidl C, Rendeiro AF, Sheffield NC, Bock C. ChIPmentation: fast, robust, low-input ChIP-seq for histones and transcription factors. *Nat Methods* **12**, 963-965 (2015).

27. Risca VI, Greenleaf WJ. Unraveling the 3D genome: genomics tools for multiscale exploration. *Trends Genet* **31**, 357-372 (2015).

28. Kundaje A*, et al.* Integrative analysis of 111 reference human epigenomes. *Nature* **518**, 317-330 (2015).

29. Stevenson FK, Krysov S, Davies AJ, Steele AJ, Packham G. B-cell receptor signaling in chronic lymphocytic leukemia. *Blood* **118**, 4313-4320 (2011).

30. Ecker S, Pancaldi V, Rico D, Valencia A. Higher gene expression variability in the more aggressive subtype of chronic lymphocytic leukemia. *Genome Med* **7**, 8 (2015).

31. Sheffield NC, Bock C. LOLA: enrichment analysis for genomic region sets and regulatory elements in R and Bioconductor. *Bioinformatics* **32**, 587-589 (2016).

32. Morabito F*, et al.* Surrogate molecular markers for IGHV mutational status in chronic lymphocytic leukemia for predicting time to first treatment. *Leuk Res* **39**, 840-845 (2015).

33. Nikitin EA*, et al.* Expression level of lipoprotein lipase and dystrophin genes predict survival in B-cell chronic lymphocytic leukemia. *Leuk Lymphoma* **48**, 912-922 (2007).

34. Forconi F*, et al.* The normal IGHV1-69-derived B-cell repertoire contains stereotypic patterns characteristic of unmutated CLL. *Blood* **115**, 71-77 (2010).

35. Mathelier A*, et al.* JASPAR 2016: a major expansion and update of the open-access database of transcription factor binding profiles. *Nucleic Acids Res*, (2015).

36. Alizadeh AA*, et al.* Toward understanding and exploiting tumor heterogeneity. *Nat Med* **21**, 846-853 (2015).

37. Sung MH, Baek S, Hager GL. Genome-wide footprinting: ready for prime time? *Nat Methods* **13**, 222-228 (2016).

38. Rosati E*, et al.* Constitutively activated Notch signaling is involved in survival and apoptosis resistance of B-CLL cells. *Blood* **113**, 856-865 (2009).

39. Tomic J, Lichty B, Spaner DE. Aberrant interferon-signaling is associated with aggressive chronic lymphocytic leukemia. *Blood* **117**, 2668-2680 (2011).

40. Mittal AK*, et al.* Role of CTLA4 in the proliferation and survival of chronic lymphocytic leukemia. *PLoS One* **8**, e70352 (2013).

41. Basso K, Margolin AA, Stolovitzky G, Klein U, Dalla-Favera R, Califano A. Reverse engineering of regulatory networks in human B cells. *Nat Genet* **37**, 382-390 (2005).

42. Lefebvre C*, et al.* A human B-cell interactome identifies MYB and FOXM1 as master regulators of proliferation in germinal centers. *Mol Syst Biol* **6**, 377 (2010).

43. Yepes S, Torres MM, Lopez-Kleine L. Regulatory network reconstruction reveals genes with prognostic value for chronic lymphocytic leukemia. *BMC Genomics* **16**, 1002 (2015).

44. Bock C*, et al.* Reference Maps of human ES and iPS cell variation enable high-throughput characterization of pluripotent cell lines. *Cell* **144**, 439-452 (2011).

45. Buenrostro JD*, et al.* Single-cell chromatin accessibility reveals principles of regulatory variation. *Nature* **523**, 486-490 (2015).

46. Jin W*, et al.* Genome-wide detection of DNase I hypersensitive sites in single cells and FFPE tissue samples. *Nature* **528**, 142-146 (2015).

47. Jiang H, Lei R, Ding SW, Zhu S. Skewer: a fast and accurate adapter trimmer for next-generation sequencing paired-end reads. *BMC Bioinformatics* **15**, 182 (2014).

48. Langmead B, Salzberg SL. Fast gapped-read alignment with Bowtie 2. *Nat Methods* **9**, 357-359 (2012).

49. Tarasov A, Vilella AJ, Cuppen E, Nijman IJ, Prins P. Sambamba: fast processing of NGS alignment formats. *Bioinformatics* **31**, 2032-2034 (2015).

50. Quinlan AR, Hall IM. BEDTools: a flexible suite of utilities for comparing genomic features. *Bioinformatics* **26**, 841-842 (2010).

51. Zhang Y*, et al.* Model-based analysis of ChIP-Seq (MACS). *Genome Biol* **9**, R137 (2008).

52. Hoffman MM*, et al.* Integrative annotation of chromatin elements from ENCODE data. *Nucleic Acids Res* **41**, 827-841 (2013).

53. Bolger AM, Lohse M, Usadel B. Trimmomatic: a flexible trimmer for Illumina sequence data. *Bioinformatics* **30**, 2114-2120 (2014).

54. Langmead B, Trapnell C, Pop M, Salzberg SL. Ultrafast and memory-efficient alignment of short DNA sequences to the human genome. *Genome Biol* **10**, R25 (2009).

55. Glaus P, Honkela A, Rattray M. Identifying differentially expressed transcripts from RNA-seq data with biological variation. *Bioinformatics* **28**, 1721-1728 (2012).

56. Love MI, Huber W, Anders S. Moderated estimation of fold change and dispersion for RNA-seq data with DESeq2. *Genome Biol* **15**, 550 (2014).

57. Ernst J, Kellis M. Large-scale imputation of epigenomic datasets for systematic annotation of diverse human tissues. *Nat Biotechnol* **33**, 364-376 (2015).

58. Rosenbloom KR*, et al.* The UCSC Genome Browser database: 2015 update. *Nucleic Acids Res* **43**, D670-681 (2015).

59. Pedregosa F*, et al.* Scikit-learn: Machine learning in Python. *The Journal of Machine Learning Research* **12**, 2825-2830 (2011).

60. Sheffield NC*, et al.* Patterns of regulatory activity across diverse human cell types predict tissue identity, transcription factor binding, and long-range interactions. *Genome Res* **23**, 777-788 (2013).

61. Sanchez-Castillo M*, et al.* CODEX: a next-generation sequencing experiment database for the haematopoietic and embryonic stem cell communities. *Nucleic Acids Res* **43**, D1117-1123 (2015).

62. Liu T*, et al.* Cistrome: an integrative platform for transcriptional regulation studies. *Genome Biol* **12**, R83 (2011).

63. Adams D*, et al.* BLUEPRINT to decode the epigenetic signature written in blood. *Nat Biotechnol* **30**, 224-226 (2012).

64. Wang B, Cunningham JM, Yang XH. Seq2pathway: an R/Bioconductor package for pathway analysis of next-generation sequencing data. *Bioinformatics* **31**, 3043-3045 (2015).

65. Sherwood RI*, et al.* Discovery of directional and nondirectional pioneer transcription factors by modeling DNase profile magnitude and shape. *Nat Biotechnol* **32**, 171-178 (2014).

66. Qu K*, et al.* Individuality and variation of personal regulomes in primary human T cells. *Cell Syst* **1**, 51-61 (2015).

67. Hagberg AA, Schult DA, Swart PJ. Exploring network structure, dynamics, and function using NetworkX. In: *Proceedings of the 7th Python in Science Conference*. eds Varoquaux G, Vaught T, Millman J (2008).

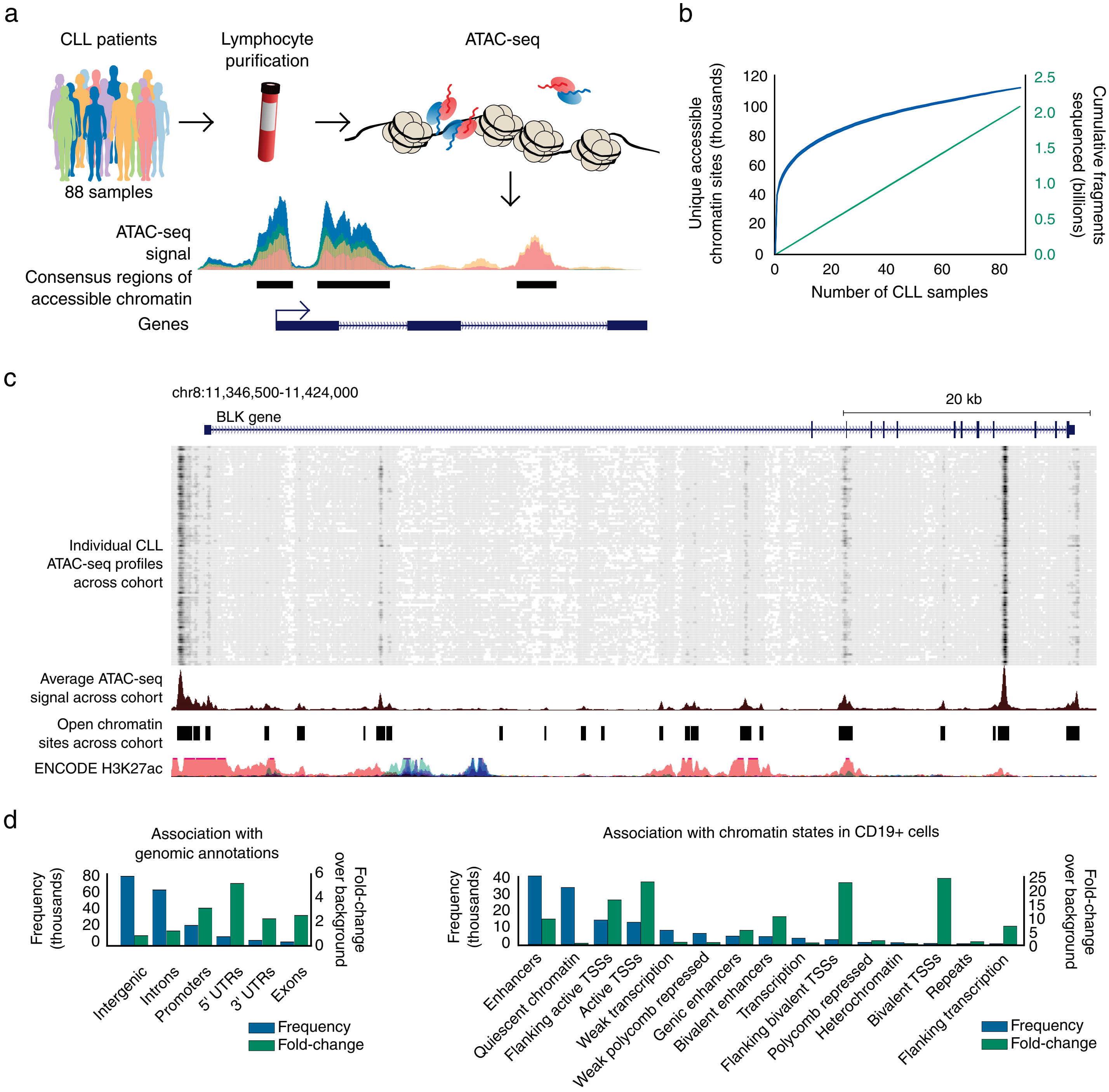
a
CLL patients
88 samples
Lymphocyte purification
ATAC-seq
ATAC-seq signal
Consensus regions of accessible chromatin
Genes
b
Unique accessible chromatin sites (thousands)
120
100
80
60
40
20
0
0
20
40
60
80
Number of CLL samples
Cumulative fragments sequenced (billions)
2.5
2.0
1.5
1.0
0.5
0.0
c
chr8:11,346,500-11,424,000
20 kb
BLK gene
Individual CLL ATAC-seq profiles across cohort
Average ATAC-seq signal across cohort
Open chromatin sites across cohort
ENCODE H3K27ac
d
Association with genomic annotations
Frequency (thousands)
80
60
40
20
0
Fold-change over background
6
4
2
0
Intergenic
Introns
Promoters
5' UTRs
3' UTRs
Exons
Frequency
Fold-change
Association with chromatin states in CD19+ cells
Frequency (thousands)
40
30
20
10
0
Fold-change over background
25
20
15
10
5
0
Enhancers
Quiescent chromatin
Flanking active TSSs
Active TSSs
Weak transcription
Weak polycomb repressed
Genic enhancers
Bivalent enhancers
Transcription
Flanking bivalent TSSs
Polycomb repressed
Heterochromatin
Bivalent TSSs
Repeats
Flanking transcription
Frequency
Fold-change

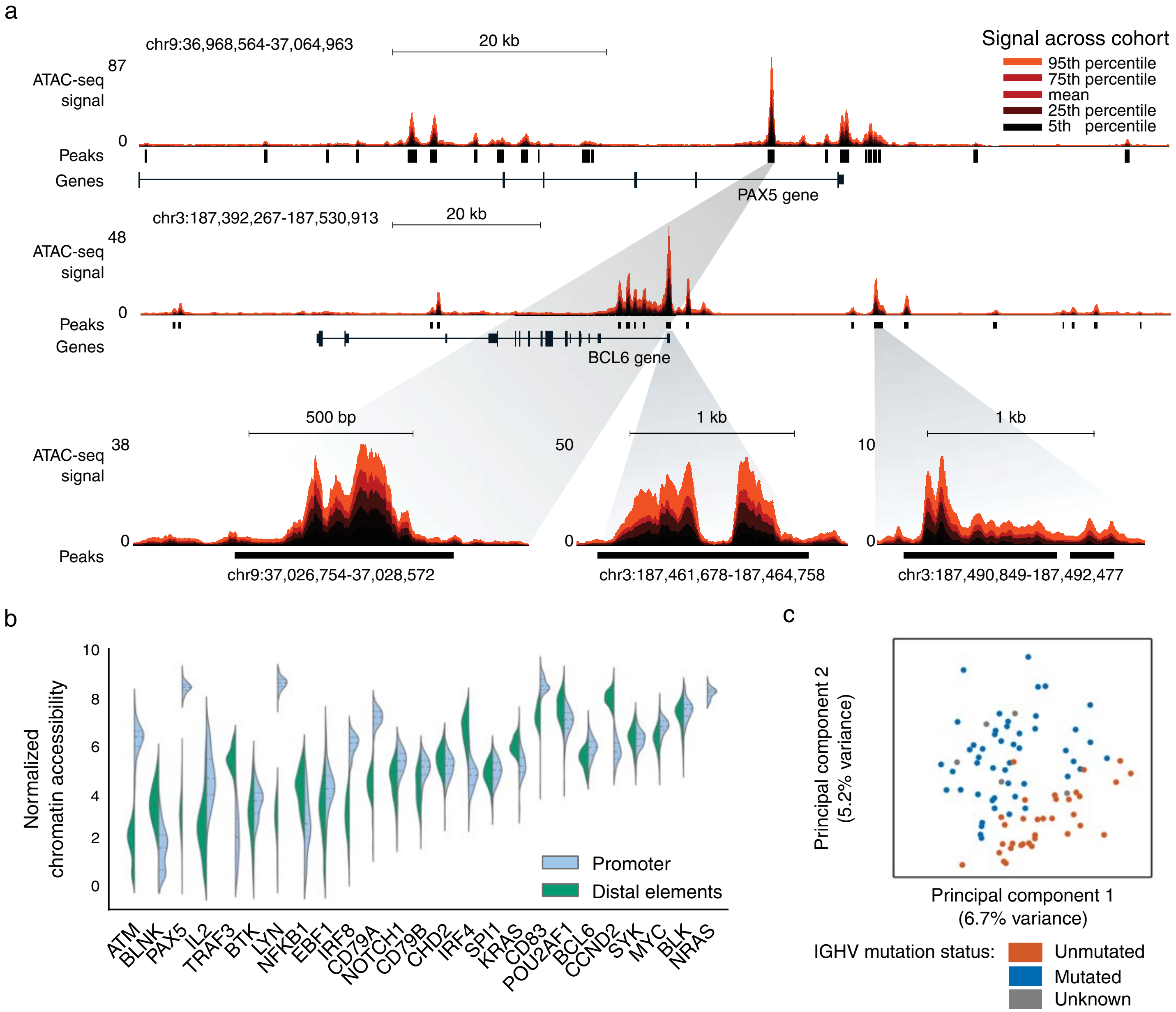
a
chr9:36,968,564-37,064,963
20 kb
Signal across cohort
95th percentile
75th percentile
mean
25th percentile
5th percentile
ATAC-seq signal
87
0
Peaks
Genes
PAX5 gene
chr3:187,392,267-187,530,913
20 kb
ATAC-seq signal
48
0
Peaks
Genes
BCL6 gene
500 bp
1 kb
1 kb
ATAC-seq signal
38
0
50
0
10
0
Peaks
chr9:37,026,754-37,028,572
chr3:187,461,678-187,464,758
chr3:187,490,849-187,492,477
b
Normalized chromatin accessibility
10
8
6
4
2
0
Promoter
Distal elements
ATM
BLNK
PAX5
IL2
TRAF3
BTK
LYN
NFKB1
EBF1
IRF8
CD79A
NOTCH1
CD79B
CHD2
IRF4
SPI1
KRAS
CD83
POU2AF1
BCL6
CCND2
SYK
MYC
BLK
NRAS
c
Principal component 2 (5.2% variance)
Principal component 1 (6.7% variance)
IGHV mutation status:
Unmutated
Mutated
Unknown

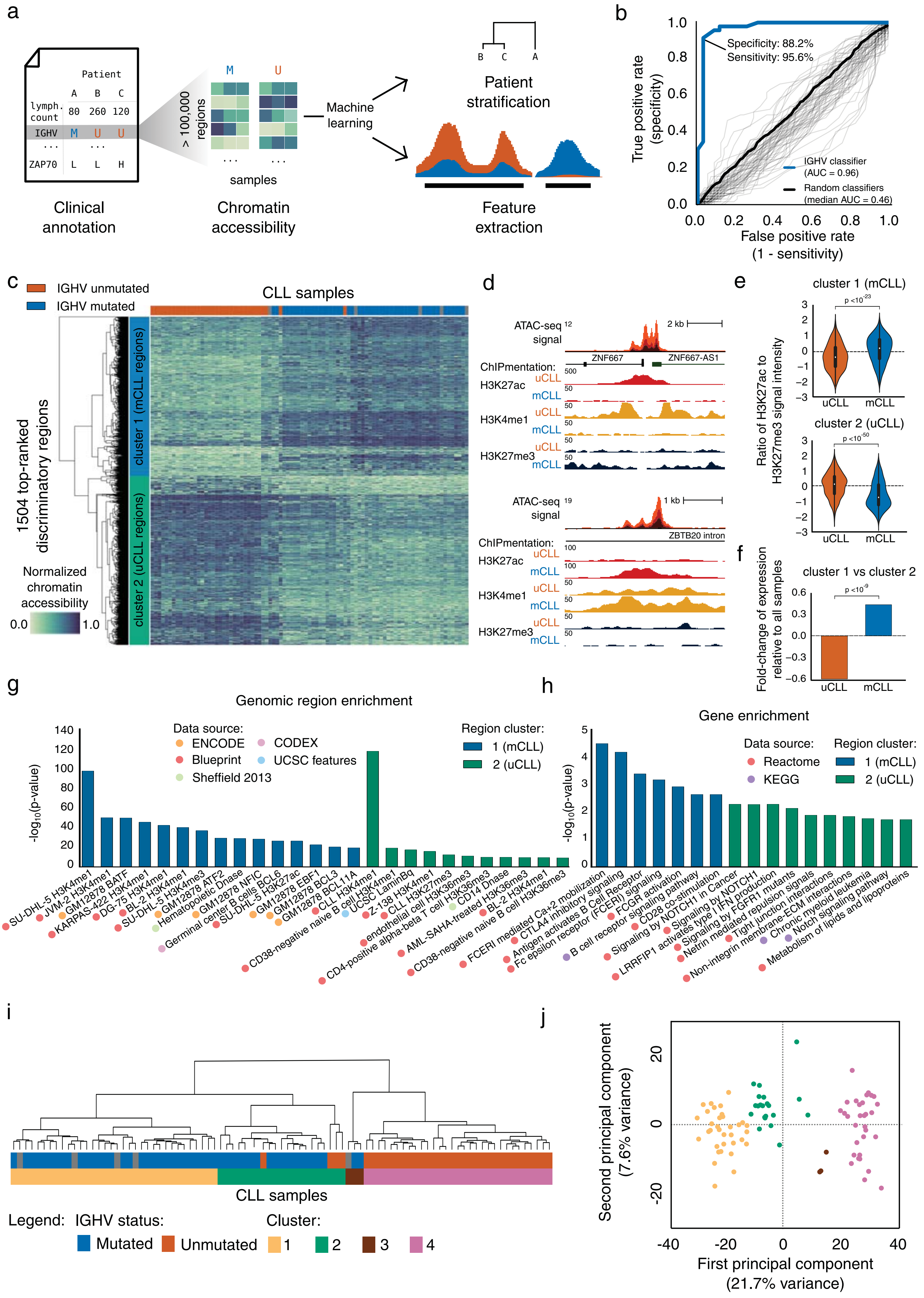
a
Patient
A B C
lymph. count 80 260 120
IGHV M U U
...
ZAP70 L L H
Clinical annotation
M
U
> 100,000 regions
samples
Chromatin accessibility
Machine learning
B C A
Patient stratification
Feature extraction
b
True positive rate (specificity)
False positive rate (1 - sensitivity)
0.0 0.2 0.4 0.6 0.8 1.0
Specificity: 88.2%
Sensitivity: 95.6%
IGHV classifier (AUC = 0.96)
Random classifiers (median AUC = 0.46)
c
IGHV unmutated
IGHV mutated
CLL samples
1504 top-ranked discriminatory regions
cluster 1 (mCLL regions)
cluster 2 (uCLL regions)
Normalized chromatin accessibility
0.0
1.0
d
ATAC-seq signal
12
2 kb
ZNF667
ZNF667-AS1
ChIPmentation:
H3K27ac
H3K4me1
H3K27me3
uCLL
mCLL
500
50
ATAC-seq signal
19
1 kb
ZBTB20 intron
100
e
cluster 1 (mCLL)
$p < 10^{-23}$
cluster 2 (uCLL)
$p < 10^{-50}$
Ratio of H3K27ac to H3K27me3 signal intensity
3 2 1 0 −1 −2 −3
uCLL mCLL
f
cluster 1 vs cluster 2
$p < 10^{-9}$
Fold-change of expression relative to all samples
0.6 0.3 0.0 −0.3 −0.6
uCLL mCLL
g
Genomic region enrichment
$-\log_{10}$(p-value)
140 120 100 80 60 40 20 0
Data source:
ENCODE
CODEX
Blueprint
UCSC features
Sheffield 2013
Region cluster:
1 (mCLL)
2 (uCLL)
SU-DHL-5 H3K4me1
JVM-2 H3K4me1
GM12878 BATF
KARPAS-422 H3K4me1
DG-75 H3K4me1
BL-2 H3K4me1
SU-DHL-5 H3K4me3
GM12878 ATF2
Hematopoietic Dnase
GM12878 NFIC
Germinal center B cells BCL6
SU-DHL-5 H3K27ac
GM12878 EBF1
GM12878 BCL3
GM12878 BCL11A
CLL H3K4me1
CD38-negative naive B cell H3K4me1
UCSC LaminBq
Z-138 H3K4me1
CLL H3K27me3
endothelial cell H3K36me3
CD4-positive alpha-beta T cell H3K36me3
CD14 Dnase
AML-SAHA-treated H3K36me3
BL-2 H3K4me1
CD38-negative naive B cell H3K36me3
h
Gene enrichment
$-\log_{10}$(p-value)
5 4 3 2 1 0
Data source:
Reactome
KEGG
Region cluster:
1 (mCLL)
2 (uCLL)
FCERI mediated Ca+2 mobilization
CTLA4 inhibitory signaling
Antigen activates B Cell Receptor
Fc epsilon receptor (FCERI) signaling
FCGR activation
B cell receptor signaling pathway
CD28 co-stimulation
Signaling by NOTCH1 in Cancer
Signaling by NOTCH1
LRRFIP1 activates type I IFN production
Signaling by FGFR1 mutants
Netrin mediated repulsion signals
Tight junction interactions
Non-integrin membrane-ECM interactions
Chronic myeloid leukemia
Notch signaling pathway
Metabolism of lipids and lipoproteins
i
CLL samples
Legend: IGHV status:
Mutated
Unmutated
Cluster:
1
2
3
4
j
Second principal component (7.6% variance)
20 0 -20
First principal component (21.7% variance)
-40 -20 0 20 40

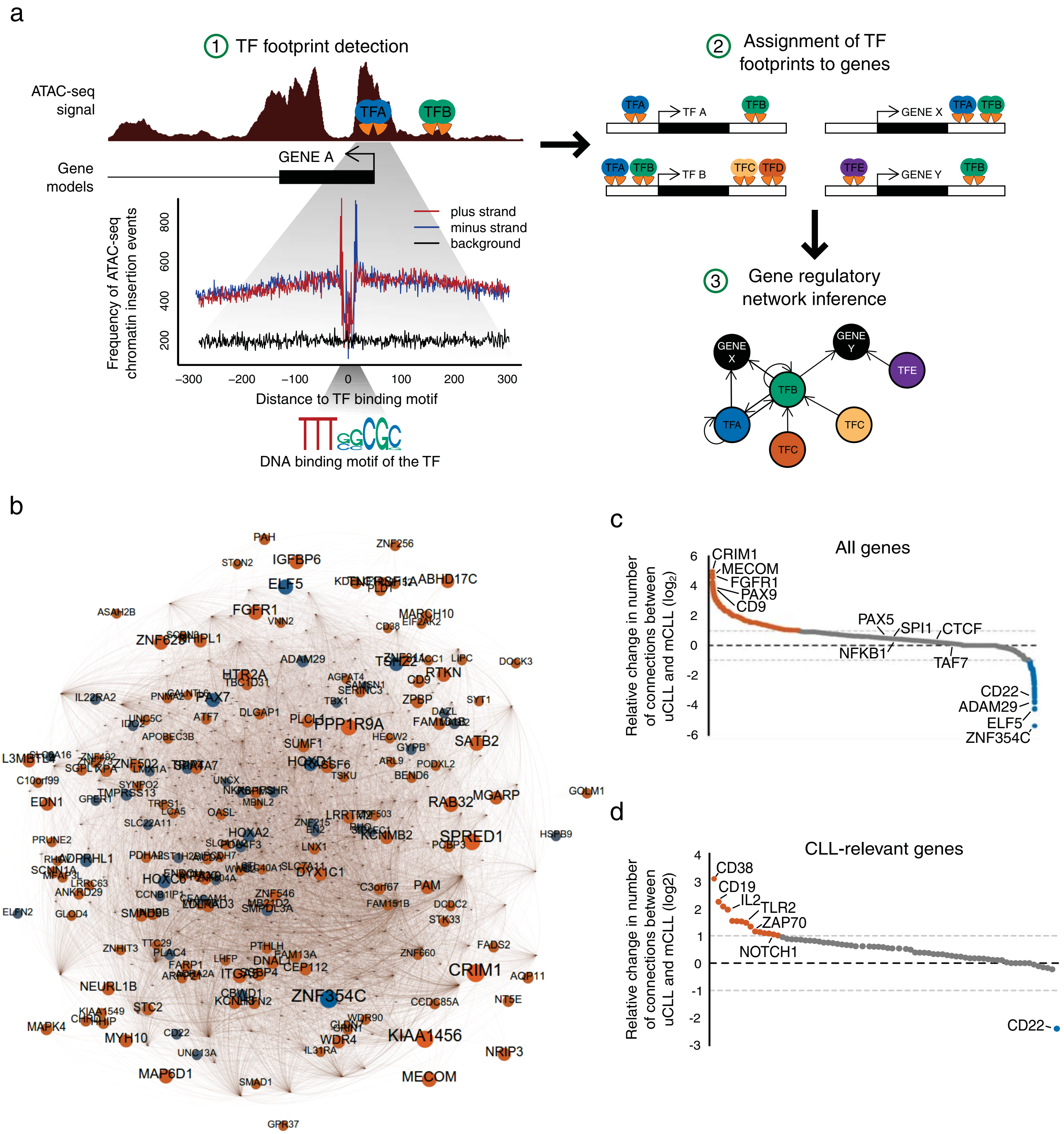
a
1 TF footprint detection
ATAC-seq signal
TFA
TFB
Gene models
GENE A
Frequency of ATAC-seq chromatin insertion events
200
400
600
800
plus strand
minus strand
background
−300
−200
−100
0
100
200
300
Distance to TF binding motif
DNA binding motif of the TF
2 Assignment of TF footprints to genes
TFA
TF A
TFB
GENE X
TFA
TFB
TF B
TFC
TFD
TFE
GENE Y
TFB
3 Gene regulatory network inference
GENE X
GENE Y
TFB
TFE
TFA
TFC
TFC
b
PAH
ZNF256
STON2
IGFBP6
ELF5
ABHD17C
ASAH2B
FGFR1
VNN2
MARCH10
EIF2AK2
CD38
ZNF628
ADAM29
TSHZ2
LIPC
DOCK3
HTR2A
TBC1D31
AGPAT4
RTKN
CD9
IL22RA2
PAX7
TBX1
ZPBP
SYT1
IDO2
UNC5C
ATF7
DLGAP1
PLCL
PPP1R9A
DAZL
APOBEC3B
HECW2
SATB2
L3MBTL4
SUMF1
GYPB
ARL9
PODXL2
C10orf99
TSKU
BEND6
UNCX
GOLM1
EDN1
GRER1
TMPRSS13
SYNPO2
MBNL2
RAB32
MGARP
TRPS1
LCA5
OASL
SLC22A11
LRRTM2
HOXA2
KCNMB2
SPRED1
HSPB9
PRUNE2
PCBP3
LNX1
ADPRHL1
HOXC8
DYX1C1
SCNN1A
ANKRD29
C3orf67
PAM
ELFN2
GLOD4
SMAD9
FAM151B
DCDC2
STK33
ZNF546
ZNHIT3
TTC29
PLAC4
PTHLH
FAM13A
ZNF660
FADS2
FARP1
LHFP
DNAI2
CEP112
CRIM1
AQP11
NEURL1B
CBWD1
ZNF354C
CCDC85A
NT5E
KIAA1549
STC2
WDR90
MAPK4
MYH10
CD22
WDR4
KIAA1456
NRIP3
UNC13A
IL31RA
MAP6D1
SMAD1
MECOM
GPR37
c
All genes
Relative change in number of connections between uCLL and mCLL (log2)
6
4
2
0
-2
-4
-6
CRIM1
MECOM
FGFR1
PAX9
CD9
PAX5
SPI1
CTCF
NFKB1
TAF7
CD22
ADAM29
ELF5
ZNF354C
d
CLL-relevant genes
Relative change in number of connections between uCLL and mCLL (log2)
4
3
2
1
0
-1
-2
-3
CD38
CD19
IL2
TLR2
ZAP70
NOTCH1
CD22